Solid-source metal-organic MBE for elemental Ir and Ru films Θ

Special Collection: Special Topic Collection Commemorating the Career of Frederick J. Walker

Sreejith Nair ➡ 📵 ; Kyle Noordhoek ⑩ ; Dooyong Lee ⑩ ; Christopher J. Bartel ➡ ⑩ ; Bharat Jalan ➡ ⑩



J. Vac. Sci. Technol. A 41, 062701 (2023) https://doi.org/10.1116/6.0002955









Solid-source metal-organic MBE for elemental Ir and Ru films

Cite as: J. Vac. Sci. Technol. A 41, 062701 (2023); doi: 10.1116/6.0002955 Submitted: 7 July 2023 · Accepted: 21 August 2023 · Published Online: 29 September 2023







Sreejith Nair, ^{1,a)} (D) Kyle Noordhoek, ¹ (D) Dooyong Lee, ^{1,2} (D) Christopher J. Bartel, ^{1,a)} (D) and Bharat Jalan ^{1,a)} (D)



AFFILIATIONS

- Department of Chemical Engineering and Materials Science, University of Minnesota-Twin Cities, Minnesota 55455
- ²Department of Physics Education, Kyungpook National University, 80, Daehak-ro, Buk-qu, Daequ 41566, South Korea

Note: This paper is part of the Special Topic Collection Commemorating the Career of Fredrick J. Walker.

^{a)}Authors to whom correspondence should be addressed: nair0074@umn.edu; cbartel@umn.edu; and bjalan@umn.edu

ABSTRACT

Thin films of elemental metals play a very important role in modern electronic nano-devices as conduction pathways, spacer layers, spin-current generators/detectors, and many other important functionalities. In this work, by exploiting the chemistry of solid metal-organic source precursors, we demonstrate the molecular beam epitaxy synthesis of elemental Ir and Ru metal thin films. The synthesis of these metals is enabled by thermodynamic and kinetic selection of the metal phase as the metal-organic precursor decomposes on the substrate surface. Film growth under different conditions was studied using a combination of *in situ* and *ex situ* structural and compositional characterization techniques. The critical role of substrate temperature, oxygen reactivity, and precursor flux in tuning film composition and quality is discussed in the context of critical role of substrate temperature, oxygen reactivity, which precursor adsorption, decomposition, and crystal growth. Computed thermodynamics quantifies the driving force for metal of page 12 precursor adsorption, decomposition, and crystal growth. Computed thermodynamics quantifies the driving force for metal of page 12 precursor adsorption, decomposition, and crystal growth. Computed thermodynamics quantifies the driving force for metal of page 12 precursor adsorption, decomposition, and crystal growth. Computed thermodynamics quantifies the driving force for metal of page 12 precursor adsorption, decomposition, and crystal growth. Computed thermodynamics quantifies the driving force for metal of page 12 precursor adsorption as a function of synthesis conditions and changes in chemical potential. These results indicate that bulk thermodynamics are a plausible origin 4 precursor adsorption as a function of synthesis conditions and changes in chemical potential. These results indicate that bulk thermodynamics are a plausible origin 4 precursor adsorption as a function of synthesis conditions and changes in chemical potential. These results indicate that bulk thermodynamics are a plausible origin 4 precursor adsorption as a function of synthesis conditions.

Published under an exclusive license by the AVS. https://doi.org/10.1116/6.0002955

I. INTRODUCTION

The platinum group metals have been investigated for decades due to their high conductivity and corrosion resistance. Thin films of metals like Ru and Ir, in particular, have been studied for applications as interconnects and diffusion barriers in microelectronics.²⁻⁴ The electronic and structural features of these metals have further led to their widespread use as catalysts for a variety of gas-phase⁵⁻⁷ and electrochemical reactions⁸ crucial for enabling sustainable technologies like the production of green hydrogen. Their high melting points, mechanical strength, and corrosion resistance have also led to their application in extreme conditions. The performance of thin film devices and electrocatalysts, however, is sensitive to the film structure and quality, which in turn depends on the synthesis technique and control over the thermodynamic and kinetic aspects of thin film growth.

Thin film growth of Ru and Ir has been studied using a wide variety of techniques like Atomic Layer Deposition (ALD), 10, Metal-Organic Chemical Vapor Deposition, 12,13 and sputtering. 14 However, to the best of our knowledge, there exists no report of MBE growth of Ru metal thin films and only one report on Ir metal thin films, 15 the primary reason being the difficulty to sublimate/evaporate pure Ru and Ir. Another important reason for the lack of interest in MBE growth of these metal films has been the difficulty for commercial scalability and high cost-to-reward ratio, in terms of both technological breakthroughs and fundamental discoveries. However, the ever-increasing quest for device miniaturization, the development of complex multilayer devices, and the discovery of strain and dimensionality-controlled emergence of topological 16 and magnetic properties in elemental metal thin films has led to renewed interest in the synthesis of ultra-thin metal films.

One of the most widely used approaches for scalable and conformal synthesis of elemental metal thin films has been the use of metal-organic precursors in techniques like ALD and CVD (typical base pressure $\sim 10^{-6}$ – 10^{-5} Torr). The metal-organic precursors are chosen such that they have the right balance of thermal and chemical stability along with a high vapor pressure. The choice of precursor not only affects the operating conditions but may also affect the choice of co-reactants for efficient decomposition of precursor and metal deposition. For example, although molecular O₂ has been the most used co-reactant, other co-reactants like O3 and H2 (sometimes in different combinations with O2) have also been employed

phology. 10,18 Co-reactants like CO (Ref. 19) have also been shown to affect the density and size of nucleating islands, thereby enabling smoother surface morphology of Ru thin films grown by CVD. Employing metal-organic precursors in an ultrahigh vacuum (UHV) technique like MBE (base pressure $\sim 10^{-10}$ – 10^{-9} Torr), however, comes with additional considerations necessary for maintaining the high purity and quality that conventional MBE offers. Nunn et al. 20,21 recently devised a new approach to deliver hard-to-sublimate metals (M) using solid metal-organic precursors ([M(acac)x], where "acac" stands for acetylacetonate and "x" denotes the number of acac ligands coordinated to the metal atom) placed in a conventional effusion cell, directly interfaced with the ultrahigh vacuum inside the MBE system. The solid precursors for Ir and Ru used in this work have low vapor pressures at room temperature essential for achieving a UHV base pressure, as shown in Table I. They also have high melting points and decomposition temperatures relative to the operating temperatures, allowing for stable and scalable flux delivery through simple resistive heating in a conventional effusion cell at temperatures less than 200 °C. This eliminates the need for complex gas inlet systems required for liquid metal-organic precursors employed in other hybrid MBE techniques^{24,25} and the use of high temperature electron beam evaporation in the case of pure Ir and Ru metal sources. Further, the use of reactive oxidants like oxygen plasma helps oxidize the organic by-products resulting in negligible hydrocarbon contamination in the film as evidenced by the excellent structural and electronic properties reported in Refs. 21 and 29 for RuO₂ and IrO2 films, respectively. Solid-source metal-organic MBE (SSMOMBE), thus, resolves a major hurdle in the MBE thin film growth of some of the platinum group metals.

to tune the phase composition, film crystallinity, and surface mor-

In this work, using Ir(acac)3 and Ru(acac)3 as the solid metalorganic source precursors, Ir and Ru thin films were grown on different orientations of TiO2 substrates using the SSMOMBE technique. We demonstrate how thermodynamic and kinetic factors like substrate temperature, activity of co-fed oxygen, and precursor flux can be tuned to obtain the desired phase composition, crystallinity, and surface morphology. The obtained results are discussed in terms of precursor chemistry, surface energetics, computational thermodynamics, and epitaxial relation to the substrates.

II. EXPERIMENT

SSMOMBE approach was employed to grow Ir and Ru films on rutile TiO2 substrates using an oxide MBE system (EVO 50, Scienta Omicron, Germany) with a base pressure of 10⁻¹⁰ Torr. Ir (acac)₃ and Ru(acac)₃ (American Elements, USA) were supplied at source temperatures of 170-175 and 185-195 °C, respectively, using low-temperature effusion cells (E-Science, Inc., USA & MBE-Komponenten, GmbH, Germany). High purity 5N oxygen was supplied using a gas inlet system equipped with a mass flow controller (MKS Instruments, Inc., USA). Activated oxygen was generated using an inductively coupled radio frequency plasma source (Mantis, UK) operated at 250 W. Oxygen, whenever supplied, created a background pressure of 5×10^{-6} Torr. All the substrates, before growth, were sequentially cleaned in acetone, methanol, and isopropanol before being subjected to a degassing step at 200 °C in the load-lock chamber of the MBE system. Before film growth, substrates were also subjected to oxygen plasma cleaning at the growth temperature. Substrates were heated via radiative heating using an SiC heater (MBE-Komponenten, GmbH, Germany).

ARTICLE

Films were characterized in situ during growth using Reflection High Energy Electron Diffraction (RHEED) (Staib Instruments, Inc., USA) to monitor how film growth proceeds with time under different conditions. Post-growth, film structure, and thickness were characterized using x-ray diffraction (XRD) and x-ray reflectivity (XRR) (Rigaku Corporation, Japan). Surface morphology was studied using atomic force microscopy (AFM) (Bruker, Inc., USA). Film composition was analyzed using x-ray photoelectron spectroscopy (XPS) (Physical Electronics, Inc., USA) equipped with an Al K_{α} source with a photon energy of 1486.6 eV. The measurement was done with an energy step size of 0.1 eV and a pass energy of 55 eV. To obtain a clean surface, an Argon gas cluster ion beam with an energy of 1 keV at an incidence angle of $\frac{30}{8}$ was performed for 30 s. We used a flood gun to compensate for $\frac{30}{8}$ the positive photoemission-induced surface charge. All XPS results 8 were calibrated using the binding energy of C-C bonding (284.8 eV) from the adventitious carbon on the surface. The Ir 4f ‡ and O 1s core-levels were fitted using the Lorentzian Asymmetric & (LA) line shapes after subtracting the Shirley background. The C 1s core-level was fitted using a combination of Gaussian and Lorentzian (GL) line shapes after subtracting the Shirley background. We did not apply any constraints to the XPS fitting except for the spin-orbit split (3 eV) of the Ir $4f_{7/2}$ and Ir $4f_{5/2}$ peaks. The detailed XPS fitting results are shown in Table I of the supplementary information.4

Density functional theory (DFT) calculations were used for the computational thermodynamic analysis. Ir (Fm $\bar{3}$ m, $2 \times 2 \times 2$ supercell), IrO₂ (P4₂/mnm), Ru (P6₃/mmc), and RuO₂ (P4₂/mnm) structures were optimized with r²SCAN (Ref. 30) using the Vienna

TABLE I. Relevant properties of interest for Ir(acac)₃ and Ru(acac)₃ precursors (from Refs. 22 and 23).

Properties	$Ir(acac)_3^{22}$	Ru(acac) ₃ ²³
Room temperature state	Solid	Solid
Melting point (°C)	270 °C	240 °C
Decomposition temperature (°C)	410 °C in vacuum	285 °C in vacuum
	220 °C in O_2	230 °C in O_2
Theoretical operating temperature (°C) for MBE (vapor pressure $\sim 10^{-5}$ – 10^{-2} Torr)	<120 °C	<160 °C
Stability	Air stable	Air stable



Ab Initio Simulation Package (VASP)^{31,32} and the projector augmented wave (PAW) method, ^{33,34} a plane wave energy cutoff of 520 eV, and a Γ-centered Monkhorst-Pack k-point grid with $25|b_i|$ discretizations along each reciprocal lattice vector, b_i .

The competition between the formation of the metal and oxide phases, M and MO_2 (M = Ir, Ru), respectively, was evaluated in terms of the formation energy, which provides the thermodynamic driving force for forming a compound from its elemental constituents. Positive formation energy indicates a thermodynamic preference for M formation and negative formation energy indicates that MO_2 formation is thermodynamically favored. Typical DFT calculations yield the internal energy, E, of the three relevant phases (M, O_2 , and MO_2), so at 0 K, the formation energy is computed as

$$\Delta E_f = E_{MO_2} - (E_M + E_{O_2}). \tag{1}$$

The 0 K DFT formation energy, $\Delta E_{\rm fr}$ has been shown to approximate the formation enthalpy at room temperature, $\Delta H_{\rm f}$ (298 K).

The formation energy concept also applies for alternative thermodynamic potentials. For an assumed closed system at constant temperature and pressure, it is most appropriate to consider the Gibbs formation energy, $\Delta G_{\rm f}$, which accounts for the effects of temperature and entropy that are absent in the treatment of $\Delta E_{\rm f}$ (or $\Delta H_{\rm f}$). The Gibbs free energy of elemental constituents ($G_{\rm M}$, $G_{\rm O2}$) was taken from tabulated experimental data, 37 while the free energies of the oxides were calculated by combining the DFT-calculated $E(0~{\rm K})$ with the descriptor developed by Bartel *et al.* 38 which

primarily accounts for the vibrational entropy of solid compounds. For a given partial pressure of oxygen, $p_{\rm O2}$, changes in the molecular oxygen chemical potential, $\Delta\mu_{\rm O2}$, can be computed using the following expression:

$$\Delta\mu_{\rm O_2} = RT ln(p_{\rm O_2}). \tag{2}$$

Here, p_{O2} (normalized with respect to a reference pressure, p_{ref} of 1 atm) is used to approximate the activity of O_2 . Allowing for a change in the chemical potential of the metal, $\Delta\mu_M$, in the treatment of G_M , leads to a final expression of ΔG_f that takes the following form:

$$\Delta G_f(\Delta \mu_M, \ \Delta \mu_{O_2}) = G_{MO_2}(T) - [G_M(T) + \Delta \mu_M + G_{O_2}(T, \ p_{ref}) + \Delta \mu_{O_2}(T, \ p_{O_2})].$$
(3)

III. RESULTS AND DISCUSSION

The chemistry of $M(\text{acac})_x$ precursors and the mechanism of film growth have been studied in previous reports on ALD growth of Ir and Ru films. ^{23,39} However, these studies were limited to a narrow range of process conditions. Overcoming this limitation, we studied Ir thin film growth under conditions of varying substrate temperatures and varying oxidation conditions by use of O_2 plasma and molecular O_2 . Films were also grown in the absence of any oxygen to study the thermally activated self-decomposition of the precursor. Figure 1(a) shows XRD 2θ - ω scans of films grown on TiO_2 (110) substrates

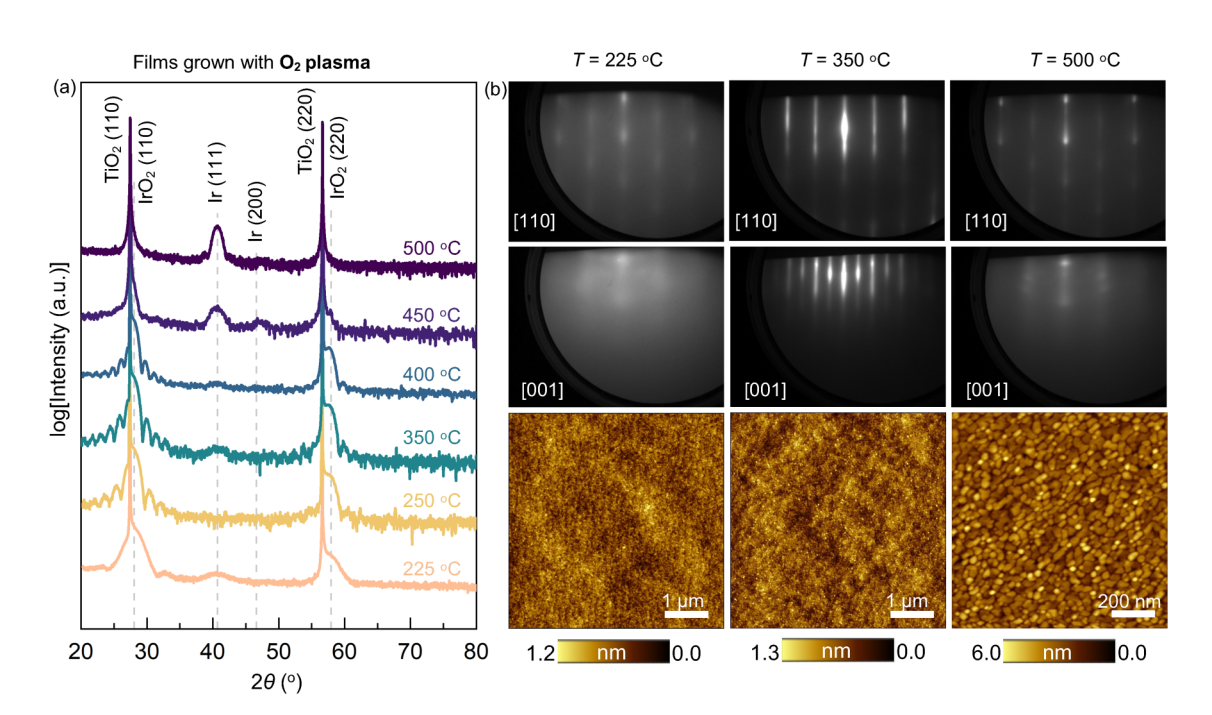


FIG. 1. (a) XRD 2θ - ω scans of films grown using Ir(acac)₃ and O₂ plasma at different substrate temperatures. (b) Corresponding post-growth RHEED images (top two rows) along two orthogonal in-plane crystallographic directions of the substrate and AFM images (bottom row) of film surface for three different substrate temperatures that represent the different film growth regimes as a function of substrate temperature.

under conditions of constant Ir(acac)₃ and O₂ plasma flux, while varying the substrate temperature. We observed that at temperatures above 225 °C, high quality single crystalline IrO2 films were obtained as evidenced by the Laue oscillations near the (110) and (220) IrO2 Bragg peaks. This is in line with reports of other MBE-grown IrO2 where 300-350 °C is found to be the most used substrate temperature. Further, we observed a transition from IrO2 to Ir metal thin films as we increased the substrate temperature above 450 °C. This transition from IrO2 to Ir is ascertained by XPS. The evolution of Ir 4f spectra shown in Fig. 2(a) clearly reflects a shift in the position of the spin–orbit split $4f^{5/2}$ and $4f^{7/2}$ peaks toward lower binding energy when the substrate temperature is increased from 400 to 450° C. The percentage film composition (extracted from the integrated peak areas) plotted as a function of substrate temperature in Fig. 2(b) summarizes how the Ir/IrO2 composition varies with substrate temperature. A pronounced shift is also observed in the valence band spectra shown in Fig. 2(c), which reflects the higher density of states at the Fermi level for Ir metal as compared to the semi-metallic IrO₂. However, as will be discussed later in terms of thermodynamics, 450° C is below the anticipated equilibrium transition from IrO₂ to Ir. This observation raises three important questions. (1) Is the apparent reduction in plasma activity during the film growth process a result of oxygen being consumed in precursor decomposition? (2) Is the discrepancy in observed plasma activity a result of the non-equilibrium nature of the epitaxial growth process? (3) Does the metal-organic precursor decrease the chemical potential of the depositing metal? A possible hypothesis to address the first two issues can be derived from the observation of Ir metal formation at temperatures above 200 °C when O₃ was used as the oxidant as reported by Hämäläinen et al.⁴¹ The Ir metal formation at such a low temperature was attributed to an increased amount of reactive O species being consumed in oxidation of the ligands and their decomposition products. Although a direct comparison between O3 used in an ALD process and O2 plasma used in a continuous deposition MBE process may not be appropriate, it is plausible that some of the activated oxygen species in the plasma are consumed in decomposing and oxidizing the ligands to CO2 and H2O, which have been previously reported to be the predominant decomposition products in the presence of oxygen by Gelfond et al.12 Further, kinetic factors could also play a role in the crossover from IrO2 to Ir since a continuous co-deposition process is sensitive to reactant fluxes, residence time of the adsorbed species on the substrate surface, adatom mobilities and reaction rates. For example, as shown in Fig. 1(a), the XRD pattern of film grown at 225 °C substrate temperature also indicates a small degree of Ir metal formation. This may arise from diminished oxygen coverage as a result of incomplete precursor decomposition and high surface coverage of precursor molecules along with high molecular weight decomposition products. The low temperature could also lead to sluggish Ir to IrO₂ kinetics and Ir buildup in the film.

For temperatures above 450 °C where the conditions are more reducing (inhibiting oxide formation), we observe that an increasing substrate temperature leads to the formation of (111) textured Ir metal, which is the most stable (lowest surface energy 42 of 2.26 J/m²) facet for cubic close packed Ir. However, as observed from the AFM image in Fig 1(b), we can see that in contrast to the atomically smooth oxide films, the Ir metal film shows significant island formation, which is also reflected in the loss of well-defined streaks

in RHEED. This has been commonly observed for the growth of metals on dielectric oxide substrates due to the low surface energy of the oxide substrates [$<1 \text{ J/m}^2$ for TiO₂ (110) surface⁴³]. The rootmean square roughness of the Ir film grown at 500 °C [shown in Fig. 1(b)] is \sim 0.7 nm despite the island-like film morphology.

To study the effect of oxygen reactivity on precursor decomposition and film growth, thin films of Ir metal were also grown at different substrate temperatures in the presence of molecular O₂. Due to the lower reactivity of molecular O2 as compared to O2 plasma, one would expect sluggish precursor decomposition and IrO₂ formation kinetics. It has also been previously reported that the oxygen activity can change the oxide decomposition threshold, which implies that the oxygen reactivity can shift the thermodynamic phase stability of the oxide.⁴⁴ Accordingly, as shown in Fig. 3(a), we observed that for the growth temperatures studied, we only detected Ir metal peaks in XRD. Interestingly, we also found increased polycrystallinity in the Ir films grown at 500 °C using molecular oxygen (in contrast to the Ir films grown at the same temperature but in oxygen plasma). Increased polycrystallinity is evident from the near equal intensity of the Ir (111) and Ir (200) peaks in XRD and increased ring-like pattern in RHEED as shown in Figs. 3(a) and 3(e), respectively. Higher substrate temperatures resulted in increased Ir (111) texture [Fig. 3(a)] and larger grain sizes [Fig. 3(b)], possibly arising from higher adatom mobilities and growth rate. 45 The film thickness as obtained from XRR (Supplementary Fig. S1)⁴⁷ also increased, suggesting that the growth rate could be governed by precursor decomposition kinetics. Substrate temperatures lower than 500 °C were not pursued since the interplay of low thermal energy and oxygen reactivity

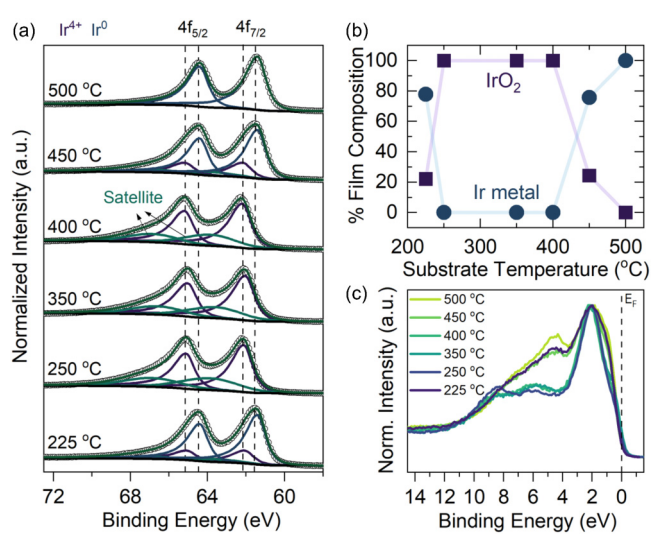


FIG. 2. (a) XPS Ir 4f spectra and peak fits for films shown in Fig. 1, which were grown at different substrate temperatures. (b) Corresponding film compositions (calculated from the integrated peak area ratios) plotted as a function of substrate temperature. (c) Corresponding valence band spectra of the films grown at different substrate temperatures, indicating a clear shift when the composition changes from oxide to metal.

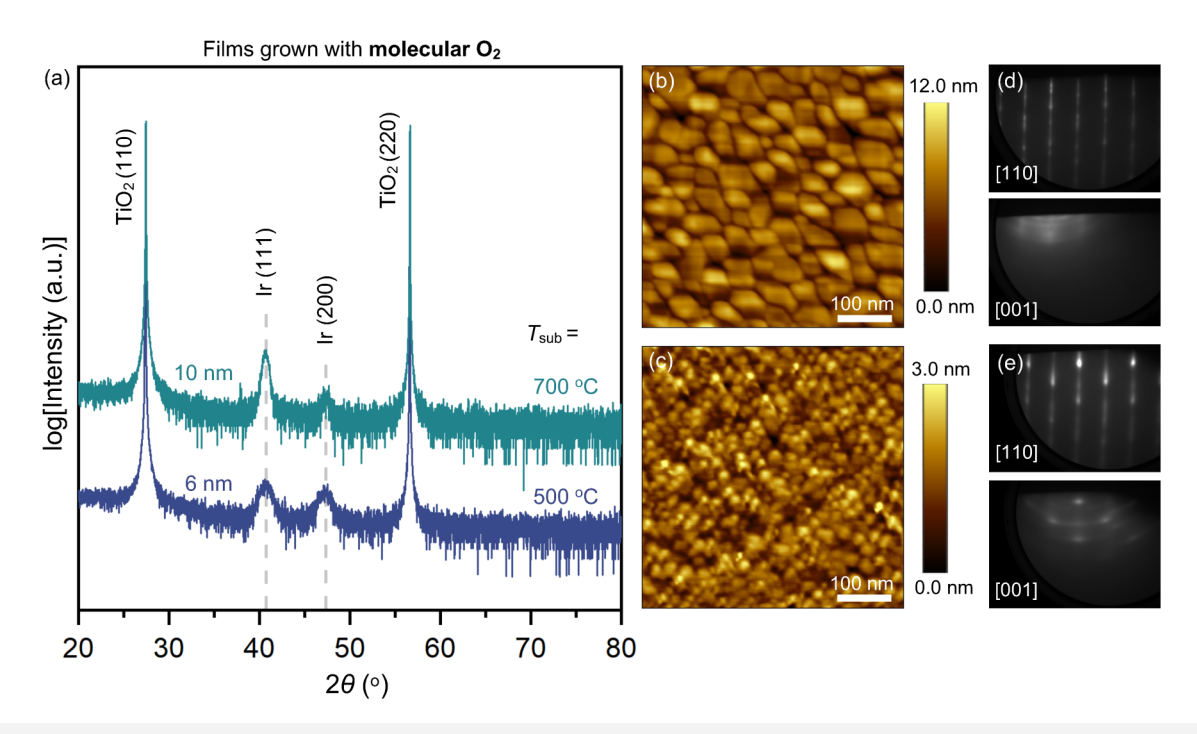


FIG. 3. (a) XRD 2θ - ω scans of films grown using Ir(acac)₃ and molecular O_2 at different substrate temperatures. Post-growth AFM images of films grown at substrate temperatures of (b) 700 and (c) 500 °C. Post-growth RHEED images along two orthogonal substrate crystallographic directions for films grown at substrate temperatures of (d) 700 and (e) 500 °C.

could lead to an even lower film growth rate and possibly poorer film quality due to sluggish growth kinetics.

The above observations of film microstructure and composition under different conditions point to an important role of precursor decomposition thermodynamics and kinetics. Hence, to understand the thermolysis behavior of the precursor and film growth in the absence of oxygen, Ir thin films were grown by sublimating Ir(acac)₃ without any additional oxygen being fed to the MBE chamber. As observed from the XRD 2θ - ω scans shown in Fig. 4(a), no film peak was observed at a substrate temperature of 400 °C. It has been reported that Ir(acac)₃ decomposes in vacuum at a temperature slightly higher than 400 °C, 22 and hence there is likely no crystalline Ir film growth below this temperature. Increasing the substrate temperature to 700 °C enhances precursor decomposition resulting in an ambiguous Ir (111) peak in XRD, the low intensity possibly resulting from low film thickness. A further increase in substrate temperature to 900 °C leads to a clear emergence of an Ir (111) peak in XRD. However, the single crystallinity in XRD is not supported by the polycrystalline rings observed in RHEED (Supplementary Fig. S2),⁴⁷ suggesting that the absence of other Bragg peaks in XRD is a result of low film thickness or textured morphology. It may be worth pointing out that for materials that tend to form islands and do not have a well-defined epitaxial relationship with the substrate, care must be taken in drawing conclusions about the crystallinity of the films, especially in the ultra-thin limit.

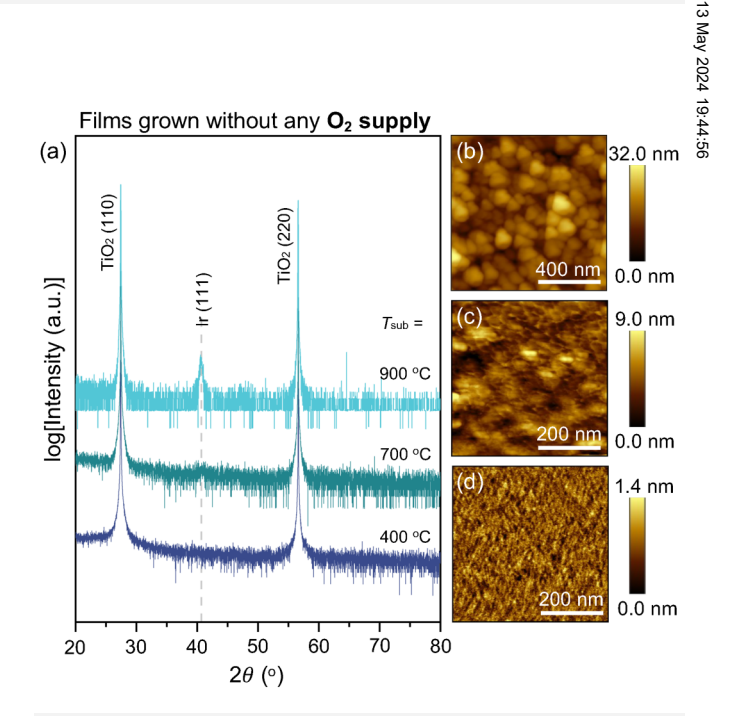


FIG. 4. (a) XRD 2θ - ω scans of films grown using Ir(acac)₃ and no O₂ supply at different substrate temperatures. Post-growth AFM images of films grown at substrate temperatures of (b) 900, (c) 700, and (d) 400 °C.



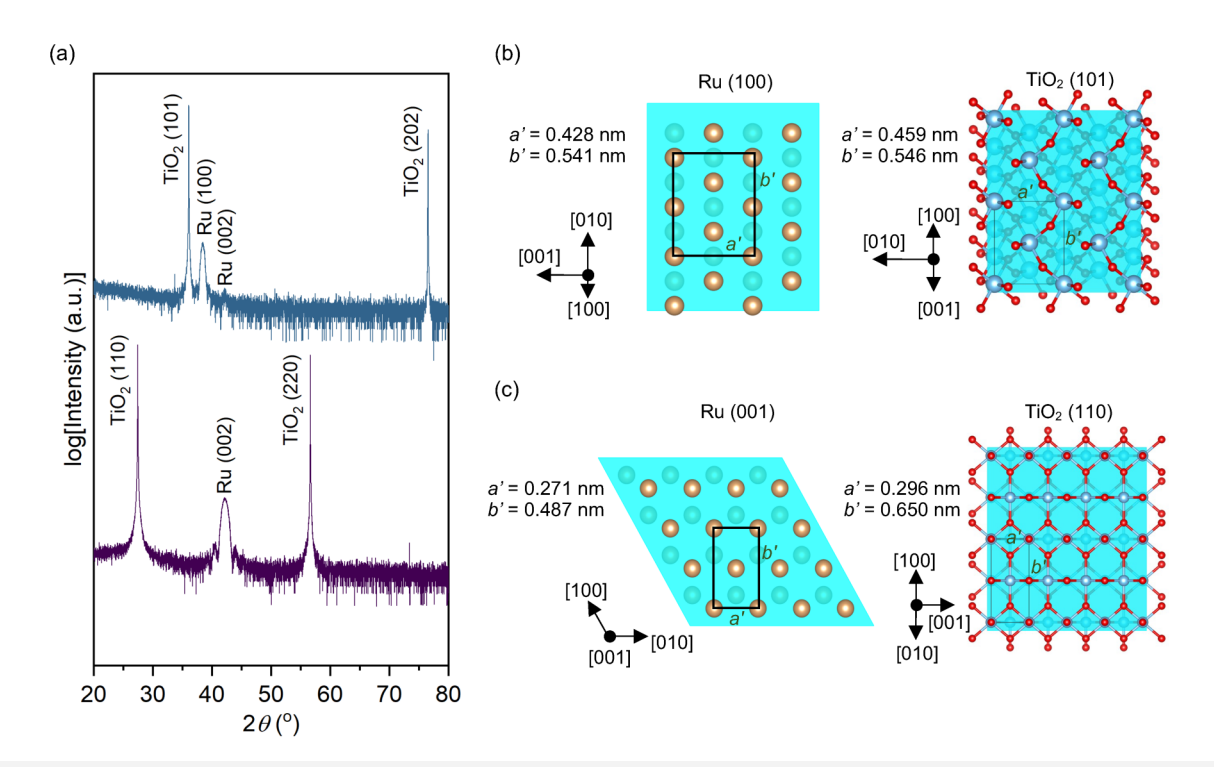


FIG. 5. (a) XRD 2θ - ω scans of films grown using higher Ru(acac)₃ flux in the presence of O_2 plasma on TiO₂ (110) and TiO₂ (101) substrates at a substrate temperature of 300 °C. Comparison of lattice constants between films and substrates where (b) Ru (100) is the dominant phase on TiO₂ (101) substrates and (c) Ru (001) is the dominant phase on TiO₂ (110) substrates. A three-dimensional view of the crystal structures can be found in Supplementary Fig. S4.

From a comparison of post-growth RHEED images for films grown under different oxidation conditions (Figs. 1 and 3; Supplementary Fig. S2),⁴⁷ it is evident that a lower oxygen reactivity leads to increased polycrystallinity. Increasing polycrystallinity with decreasing oxygen reactivity is also accompanied by a higher substrate temperature requirement for the onset of film growth. This suggests that the increased polycrystallinity could be related to the precursor decomposition process. A higher lifetime of adsorbed precursor molecules can limit adatom mobilities and access to favorable crystal nucleation and growth sites, thereby kinetically forcing the grains to grow along facets that have a higher surface free energy. An alternative way to obtain highly oriented thin films is through the selection of a substrate that can support the epitaxial growth of the metal film. For example, highly oriented Ir (111) films have been previously grown on c-Al2O3 substrates because of the relatively small lattice mismatch $(\sim 3\%)^{15}$ using conventional MBE. A similar result has also been previously reported for Ir metal using SSMOMBE.²⁹ Lattice-matched substrates allow control of the preferred out-of-plane growth orientation, thereby exposing different facets (that may have higher free energy) in a controlled fashion. Here, we demonstrate this orientation control by growing Ru metal on different orientations of TiO2 substrates. Ru metal was deposited at a substrate temperature of 300 °C using Ru(acac)₃ and O₂ plasma on TiO₂ (110) and TiO₂ (101) substrates. Under these conditions, RuO2 should be the thermodynamically preferred phase, yet Ru can be selectively grown by increasing the Ru flux, thereby kinetically selecting the Ru metal phase. In Supplementary Fig. S3, 47 a gradual increase in Ru cell temperature (thereby increasing Ru flux) for a given oxygen plasma flux leads to a shift from phase-pure RuO₂ to phase-pure Ru. Accordingly, as shown in Fig 5(a), Ru film grown on TiO₂ (110) substrates (stabilized using higher Ru flux as shown in Supplementary Fig. S3) 47 shows a strong preference for the (001) facet along the out-of-plane direction due to the low surface energy of the (001) facet of hexagonal close packed Ru metal [~2.624 J/m² (Ref. 46)]. However, under the same growth conditions, Ru metal shows a preferred (100) texture when grown on TiO₂ (101) substrates because of the relatively better lattice match as shown in Figs. 5(b) and 5(c).

To contextualize the experimental findings, we computed the thermodynamics of metal and oxide formation across a range of experimentally accessible growth conditions. In Fig. 6, we show $\Delta G_{\rm f}$ for the $M/M{\rm O}_2$ systems ($M={\rm Ir}$, Ru), as a function of oxygen partial pressure ($p_{{\rm O}2}$) and temperature (T), where $\Delta G_{\rm f} < 0$ indicates a thermodynamic preference for the oxide and $\Delta G_{\rm f} > 0$ indicates the metal is thermodynamically favored to form. As expected, the computed thermodynamics depict that $M{\rm O}_2$ formation becomes more favorable as $p_{{\rm O}2}$ increases or T decreases (oxidizing conditions), while the formation of M becomes more favorable as $p_{{\rm O}2}$ decreases or T increases (reducing conditions). The $\Delta G_{\rm f} = 0$ boundary separates regions of favorable M and $M{\rm O}_2$ formation and is

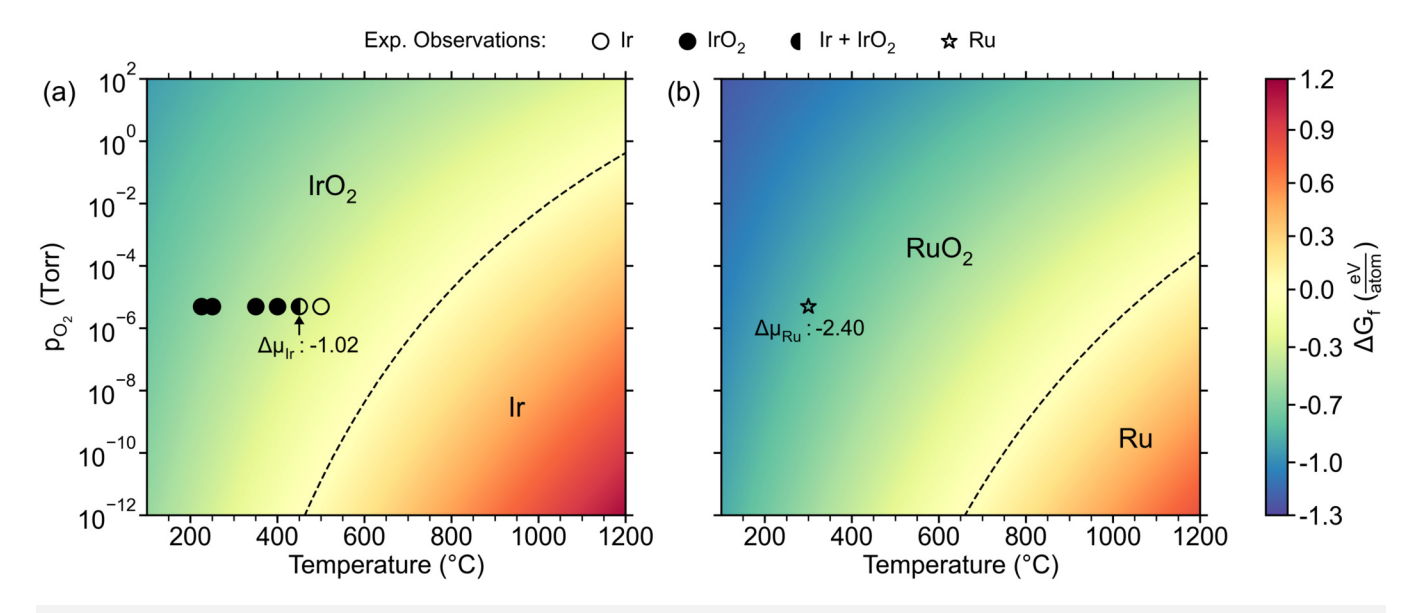


FIG. 6. Contour plots of $\Delta G_{\rm f}$ for bulk (a) Ir/IrO₂ and (b) Ru/RuO₂ as functions of T and $\rho_{\rm O2}$, ranging from 100 to 1200 °C and 1 × 10⁻¹² to 1 × 10² Torr, respectively. The $\Delta G_f = 0$ boundary is indicated by the black dashed line. For $\Delta G_f < 0$, the oxide is thermodynamically favored, whereas $\Delta G_f > 0$ favors metal formation. In (a), filled circles indicate the observed formation of IrO₂ and empty circles indicate the observed formation of Ir. The $\Delta\mu_{\rm Ir}$ required to shift $\Delta G_{\rm f}$ to 0 is indicated at T = 450 °C and $p_{O2} = 5 \times 10^{-6}$ Torr. In (b), only one set of conditions was used for the Ru/RuO₂ system in this work (yielding Ru), and these are indicated by the star. The $\Delta\mu_{Ru}$ required to shift ΔG_f to 0 is indicated at T = 300 °C and $p_{O2} = 5 \times 10^{-6}$ Torr.

indicated by the black dashed line, with each respective region labeled to the left/above (MO2 preferred) and right/below (M preferred) the black dashed line. The experiments performed in this work are shown in Fig. 6 to indicate the observed phases at these (approximate) growth conditions.

Experimentally, significant Ir formation was observed at a minimum temperature of 450 °C using an O2 plasma background pressure of 5×10^{-6} Torr [Fig. 1(a)]. In contrast, ΔG_f at 450 °C and 5×10^{-6} Torr is calculated here to be -0.34 eV/atom, indicating a small thermodynamic driving force to form IrO2. At $p_{O2} = 5 \times 10^{-6}$ Torr, Fig. 6(a) indicates that Ir formation becomes favorable ($\Delta G_f > 0$) only above 750 °C. The discrepancies between the computed and observed Ir/IrO2 transition temperatures, 750° C (computed) as opposed to 450 °C (observed), may result from a decrease in oxygen activity or a decrease in the chemical potential of Ir. As discussed previously, the use of O2 plasma is expected to increase the activity of oxygen when compared to molecular O2, further driving the formation of IrO2, though the activated oxygen could be consumed by ligand oxidation and by-product decomposition. For the increased amount of reactive oxygen species to be consumed to an extent that would produce the observed shift in the Ir/IrO2 transition temperature (down to 450 °C), an effective $p_{\rm O2}$ of 10^{-12} Torr would be required. Alternatively (or additionally), a change in chemical potential relative to elemental Ir metal, $\Delta \mu_{\rm Ir}$, could also drive the formation of Ir at low temperatures. As indicated in Fig. 6(a), $\Delta \mu_{\rm Ir} = -1.02 \, {\rm eV/atom}$ would be necessary to stabilize Ir at 450 °C and $p_{O2} = 5 \times 10^{-6}$ Torr. The use of a metal-organic complex as opposed to an elemental metal precursor may be responsible for decreasing the chemical potential of the metal. While either a decrease in the O_2 or Ir activity seems $\mathbb{R}^{\frac{1}{2}}$ plausible as a bulk thermodynamic origin for the observed lowtemperature Ir formation [Fig. 1(a)], the effects of kinetics (i.e., § preferential growth rates) or interfacial thermodynamics also $\frac{1}{2}$ cannot be ruled out.

In Fig. 6(b), we present the same analysis for the Ru/RuO₂ & system. As with Ir/IrO_2 , decreasing p_{O2} or increasing T thermodynamically favors Ru formation. However, as seen by comparison between Figs. 6(a) and 6(b), the region for which Ru is thermodynamically favored ($\Delta G_f > 0$) is much smaller than that of Ir. Experimentally, Ru metal formation was observed at 300 °C using O_2 plasma and a background pressure of 5×10^{-6} Torr [Fig. 5(a)]. In contrast, ΔG_f at 300 °C and 5×10^{-6} Torr was calculated to be -0.8 eV/atom, over twice as large as ΔG_f for Ir/IrO₂ at 450 °C, indicating a much greater thermodynamic driving force to form RuO₂. At $p_{O2} = 5 \times 10^{-6}$ Torr, Fig. 6(b) indicates that Ru formation becomes thermodynamically favorable only above 1050 °C. As was discussed with Ir/IrO2, a decrease in oxygen activity or Ru chemical potential may be responsible for the observed Ru formation when RuO2 is significantly favored. For a decrease in oxygen activity to be the cause, consumption of the activated oxygen species would need to produce an effective $p_{O2} = 10^{-25}$ Torr (at 300 °C), significantly lower than that which is achievable by MBE and orders of magnitude lower than what was calculated for the Ir/IrO2 system. Alternatively, as indicated in Fig. 6(b), $\Delta\mu_{Ru} = -2.40 \text{ eV/atom}$ would be necessary to stabilize Ru at 300 °C, over twice as large as the $\Delta u_{\rm Ir}$ required to stabilize Ir at 450 °C and $p_{\rm O2} = 5 \times 10^{-6}$ Torr. These results suggest that the formation of Ru at 300 °C may occur by a different mechanism than the formation of Ir at 450 °C.



While thermodynamic factors plausibly explain the formation of Ir at low temperatures, it is likely that thermodynamics are not sufficient to explain the preferential formation of Ru at low temperatures. Instead, the relative kinetics of Ru and RuO2 growth likely plays a major role in the formation of Ru during these lowtemperature MBE experiments.

IV. CONCLUSION

In conclusion, we have demonstrated the use of solid-source metal-organic MBE for the synthesis of thin films of elemental Ir and Ru, which find applications in catalysis and various electronic and spintronic devices due to their conducting and noble metal characteristics. We have shown how different factors like substrate temperature, oxygen reactivity, and choice of substrate can be used to tune the film composition, crystallinity, and surface morphology. The thermal decomposition of the precursor was shown to play a major role in film growth and tuning the decomposition process significantly affects the resulting film properties. We also demonstrated the ability to tune the out of plane orientation of metal films by means of substrate imposed epitaxial constraints. Thermodynamic calculations indicate that bulk thermodynamics could plausibly explain the observed Ir deposition at low temperatures. In contrast, these calculations do not adequately explain the low-temperature formation of Ru, suggesting preferential growth rates (e.g., kinetics) play a significant role in this system. Our work on MBE growth of elemental films using metal-organic precursors, thus, establishes this technique as a viable and scalable approach to synthesize these materials.

ACKNOWLEDGMENTS

Film growth and characterization (S.N. and D.L.) was supported by the U.S. Department of Energy through No. DE-SC0020211. K.N., B.J., and C.B. were supported by the UMN MRSEC program under Award No. DMR-2011401. Parts of this work were carried out at the Characterization Facility, University of Minnesota, which receives partial support from the National Science Foundation (NSF) through the MRSEC program under Award No. DMR-2011401. The authors acknowledge the Minnesota Supercomputing Institute (MSI) at the University of Minnesota for providing resources that contributed to the research results reported within this paper.

AUTHOR DECLARATIONS

Conflict of Interest

The authors have no conflicts to disclose.

Author Contributions

Sreejith Nair: Conceptualization (equal); Data curation (equal); Formal analysis (equal); Investigation (equal); Methodology (equal); Validation (equal); Visualization (equal); Writing - original draft (equal). Kyle Noordhoek: Conceptualization (equal); Data curation (equal); Formal analysis (equal); Investigation (equal); Methodology (equal); Validation (equal); Visualization (equal); Writing - original draft (equal). Dooyong Lee: Data curation (equal); Formal analysis (equal); Investigation (equal); Methodology (equal); Validation (equal); Visualization (equal); Writing - original draft (equal). Christopher J. Bartel: Conceptualization (equal); Data curation (equal); Formal analysis (equal); Funding acquisition (equal); Investigation (equal); Project administration (equal); Supervision (equal); Validation (equal); Visualization (equal); Writing - original draft (equal). Bharat Jalan: Conceptualization (equal); Data curation (equal); Formal analysis (equal); Funding acquisition (equal); Investigation (equal); Project administration (equal); Supervision (equal); Writing - original draft (equal).

DATA AVAILABILITY

The data that support the findings of this study are available within the article and its supplementary material.

REFERENCES

- ¹A. S. Darling, Int. Metall. Rev. 18, 91 (1973).
- ²L. G. Wen et al., ACS Appl. Mater. Interfaces 8, 26119 (2016).
- ³T. Zhan et al., ACS Appl. Mater. Interfaces 14, 7392 (2022).
- ⁴Y. H. Lim, H. Yoo, B. H. Choi, J. H. Lee, H.-N. Lee, and H. K. Lee, Phys. Status Solidi C 8, 891 (2011).
- ⁵A. Basinska, T. P. Maniecki, and W. K. Jozwiak, React. Kinet. Catal. Lett. 89,
- ⁶K. Fujimoto, M. Kameyama, and T. Kunugi, J. Catal. 61, 7 (1980).
- ⁷K. Liu, A. Wang, and T. Zhang, ACS Catal. 2, 1165 (2012).
- ⁸T. Reier, M. Oezaslan, and P. Strasser, ACS Catal. 2, 1765 (2012).
- 9B. Fischer, A. Behrends, D. Freund, D. F. Lupton, and J. Merker, Platinum Met.
 Rev. 43(1), 18–28 (1999). Rev. 43(1), 18-28 (1999).
- 10 T. Aaltonen, M. Ritala, Y.-L. Tung, Y. Chi, K. Arstila, K. Meinander, and M. Leskela, J. Mater. Res. 19, 3353 (2004).
- M. Leskela, J. Mater. Res. **19**, 3353 (2004).

 11 J. M. Hwang *et al.*, J. Mater. Chem. C **9**, 3820 (2021).

 12 N. V. Gelfond, N. B. Morozova, P. P. Semyannikov, S. V. Trubin, & I. K. Igumenov, A. K. Gutakovskii, and A. V. Latyshev, J. Struct. Chem. 53, 715
- 13N. B. Morozova, N. V. Gelfond, P. P. Semyannikov, S. V. Trubin, I. K. Igumenov, A. K. Gutakovskii, and A. V. Latyshev, J. Struct. Chem. 53, 725
- ¹⁴M. A. El Khakani, M. Chaker, and B. Le Drogoff, J. Vac. Sci. Technol. A 16,
- ¹⁵A. Dangwal Pandey et al., J. Appl. Phys. **120**, 075304 (2016).
- 16 L. D. Anh, K. Takase, T. Chiba, Y. Kota, K. Takiguchi, and M. Tanaka, Adv. Mater. 33, 2104645 (2021).
- 17P. Quarterman et al., Nat. Commun. 9, 2058 (2018).
- 18 J. Hämäläinen, E. Puukilainen, M. Kemell, L. Costelle, M. Ritala, and M. Leskelä, Chem. Mater. 21, 4868 (2009).
- ¹⁹W. Liao and J. G. Ekerdt, J. Vac. Sci. Technol. A 34, 041514 (2016).
- 20 W. Nunn, A. K. Manjeshwar, J. Yue, A. Rajapitamahuni, T. K. Truttmann, and B. Jalan, Proc. Natl. Acad. Sci. 118, e2105713118 (2021).
- ²¹W. Nunn, S. Nair, H. Yun, A. K. Manjeshwar, A. Rajapitamahuni, D. Lee, K. A. Mkhoyan, and B. Jalan, APL Mater. 9, 091112 (2021).
- 22K. I. Karakovskaya, S. I. Dorovskikh, E. S. Vikulova, I. Y. Ilyin, K. V. Zherikova, T. V. Basova, and N. B. Morozova, Coatings 11, 78 (2021).
- 23 I. K. Igumenov, P. P. Semyannikov, S. V. Trubin, N. B. Morozova, N. V. Gelfond, A. V. Mischenko, and J. A. Norman, Surf. Coat. Technol. 201, 9003 (2007).
- ²⁴B. Jalan, R. Engel-Herbert, N. J. Wright, and S. Stemmer, J. Vac. Sci. Technol. A 27, 461 (2009).
- ²⁵W. Nunn, T. K. Truttmann, and B. Jalan, J. Mater. Res. **36**, 4846 (2021).



- ²⁶J. K. Kawasaki, D. Baek, H. Paik, H. P. Nair, L. F. Kourkoutis, D. G. Schlom, and K. M. Shen, Phys. Rev. Mater. 2, 054206 (2018).
- ²⁷H. P. Nair et al., APL Mater. **6**, 101108 (2018).
- ²⁸M. Uchida, W. Sano, K. S. Takahashi, T. Koretsune, Y. Kozuka, R. Arita, Y. Tokura, and M. Kawasaki, Phys. Rev. B 91, 241119(R) (2015).
- ²⁹S. Nair et al., Nat. Nanotechnol. 18, 1005 (2023).
- ³⁰J. W. Furness, A. D. Kaplan, J. Ning, J. P. Perdew, and J. Sun, J. Phys. Chem. Lett. 11, 8208 (2020).
- $^{\bf 31}$ G. Kresse and J. Furthmüller, Comput. Mater. Sci. ${\bf 6}$, 15 (1996).
- **32**G. Kresse and J. Furthmüller, Phys. Rev. B **54**, 11169 (1996).
- 33 P. E. Blöchl, Phys. Rev. B 50, 17953 (1994).
- 34G. Kresse and D. Joubert, Phys. Rev. B 59, 1758 (1999).
- 35C. J. Bartel, J. Mater. Sci. 57, 10475 (2022).
- ³⁶C. J. Bartel, A. W. Weimer, S. Lany, C. B. Musgrave, and A. M. Holder, npj Comput. Mater. 5, 4 (2019).

- ³⁷I. Barin, *Thermochemical Data of Pure Substances* (VCH Publishers, Inc., New York, 1995), pp. 33–34.
- ³⁸C. J. Bartel *et al.*, Nat. Commun. **9**, 4168 (2018).
- 39 K. Knapas and M. Ritala, Chem. Mater. 23, 2766 (2011).
- 40 J. K. Kawasaki *et al.*, Phys. Rev. Lett. **121**, 176802 (2018).
- ⁴¹J. Hämäläinen, M. Kemell, F. Munnik, U. Kreissig, M. Ritala, and M. Leskelä, Chem. Mater. 20, 2903 (2008).
- ⁴²K. Klyukin, A. Zagalskaya, and V. Alexandrov, J. Phys. Chem. C 122, 29350 (2018).
- ⁴³H. Perron, C. Domain, J. Roques, R. Drot, E. Simoni, and H. Catalette, Theor. Chem. Acc. 117, 565 (2007).
- 44 A. Sawa, H. Obara, and S. Kosaka, Appl. Phys. Lett. 64, 649 (1994).
- ⁴⁵I. E. Merkulova, J. Phys.: Conf. Ser. **2119**, 012121 (2021).
- 46 P. Zhao et al., ACS Catal. 9, 2768 (2019).
- 47 See supplementary material online for film thickness, RHEED patterns, rate-dependent growth of Ru/RuO₂ films, and crystal structures of Ir, Ru, and TiO₂.